How to cite: *Angew. Chem. Int. Ed.* **2024**, *63*, e202412643
doi.org/10.1002/anie.202412643

COFs for Catalysis | Hot Paper

Chiral Ligand-Decorated Rhodium Nanoparticles Incorporated in Covalent Organic Framework for Asymmetric Catalysis

*Jiangtao Yu, Ge Yang, Ming-Liang Gao, He Wang, and Hai-Long Jiang**

Abstract: While metal nanoparticles (NPs) have demonstrated their great potential in catalysis, introducing chiral microenvironment around metal NPs to achieve efficient conversion and high enantioselectivity remains a long-standing challenge. In this work, tiny Rh NPs, modified by chiral diene ligands (Lx) bearing diverse functional groups, are incorporated into a covalent organic framework (COF) for the asymmetric 1,4-addition reactions between arylboronic acids and nitroalkenes. Though Rh NPs hosted in the COF are inactive, decorating Rh NPs with Lx creates the active Rh–Lx interface and induces high activity. Moreover, chiral microenvironment modulation around Rh NPs by altering the groups on chiral diene ligands greatly optimizes the enantioselectivity (up to 95.6% ee). Mechanistic investigations indicate that the formation of hydrogen-bonding interaction between Lx and nitroalkenes plays critical roles in the resulting enantioselectivity. This work highlights the significance of chiral microenvironment modulation around metal NPs by chiral ligand decoration for heterogeneous asymmetric catalysis.

Introduction

Chirality is an important feature related to life, which has broad application prospects in pharmaceutical, agrichemical, and fine chemical industries.[1] Enantiomers, such as thalidomide, with similar physical properties, can exhibit dramatically different biological activities or toxicity.[1a] Presently, good catalytic enantioselectivity is mostly achieved by homogeneous asymmetric catalysts, as they are able to preferentially stabilize the specific transition state of a single enantiomer. Traditional homogeneous chiral catalysts, such as salen complexes, phosphoric acid ligands, and chiral amines, have been demonstrated to be very promising in chiral conversion.[2] Unfortunately, difficulties in recycling and separation of homogeneous catalysts bring challenges to their practical applications. In recent years, heterogeneous asymmetric catalysis has garnered widespread attention due to its advantages, including the easy separation and purification of products and the reusability of catalysts, compared to homogeneous catalysis. To achieve this, the heterogenization of the aforementioned homogeneous chiral catalysts is a common and well-adopted strategy to inherit high activity and excellent enantioselectivity.[3–5] Unfortunately, their tedious synthesis processes are usually unavoidable, which require a large amount of time on synthesis and excellent synthesis skills.[5c,d]

To meet this challenge, enzyme catalysis can provide important inspiration. High activity and specific selectivity can be achieved by enzymes due to the favorable microenvironment around catalytic sites. This microenvironment creates non-covalent interactions that play critical roles in collaboration with the catalytic center, promoting the catalysis.[6] Inspired by the binding pocket in enzyme catalysis, the creation of chiral microenvironment around catalytic sites might be a feasible strategy for converting common achiral to chiral catalysts.[6c] Following this idea, the introduction of particular chiral microenvironment around catalytic sites would be able to achieve enantioselectivity. Given supported metal catalysts, such as Pt, Pd, Au, Ni, and Rh NPs, are widely applied in various industrial chemical reactions, they can be decorated with diverse chiral ligands through this strategy to afford chiral supported metal catalysts.[7] Although quite a few chiral supported metal catalysts have been reported, the majority exhibit high activity yet low enantioselectivity.[7e–h] The possible reason may lie in the background reactions caused by the high activity of metal NPs alone and the lack of effective interactions between the chiral ligands and substrates, which hinder the successful transmission of chirality.[7e–i] Therefore, it is necessary to suppress the background reaction and create non-covalent interactions such as hydrogen-bonding interactions in the chiral microenvironment, the latter of which might induce substrate activation in a particular direction or orientation to catalytic sites, thereby promoting enantioselectivity.

On the other hand, for supported metal catalysts, small metal nanoparticles (NPs) with abundant surface catalytic sites are highly desired. However, they are prone to aggregate owing to the high surface energies, giving rise to poor activity. Porous scaffolds, such as metal–organic frameworks (MOFs), zeolites, and porous carbons, have been demonstrated to be promising hosts for stabilizing metal NPs.[8] Covalent organic frameworks (COFs), a relatively new class of crystalline porous material constructed of organic linkers, featuring well-defined and tailored structures as well as high surface area,[9] would be promising

[*] J. Yu, Dr. G. Yang, Dr. M.-L. Gao, Dr. H. Wang, Prof. Dr. H.-L. Jiang
Hefei National Research Center for Physical Sciences at the Microscale, Department of Chemistry, University of Science and Technology of China, Hefei, Anhui 230026 (P. R. China)
E-mail: jianglab@ustc.edu.cn
Homepage: http://mof.ustc.edu.cn/

© 2024 Wiley-VCH GmbH

hosts for the stabilization of small metal NPs. Despite the congenital advantages, to our knowledge, related reports on COFs incorporating metal NPs remain very limited.[10] Considering that Schiff-base units are ready to chelate metal ions,[11] the fabrication of COFs involves Schiff-base units to capture and diperse metal ions, which might help to suppress the agglomeration of resulting metal NPs in the subsequent reduction process.

Bearing the above in mind, in this work, tiny Rh NPs are confined in a two-dimensional (2D) mesoporous imide-linked COF. A series of chiral diene ligands, denoted as L1, L2, and L3, respectively, with the same bicyclo-[2.2.2]octadiene structures but different functional groups, including NH^{t}Bu, 2-naphthoxy, and NMe^{t}Bu, are modified onto the Rh NPs to give Rh–Lx@COF (x=1, 2, 3) (Scheme 1). The 2D structure of the COF allows the N atoms in adjacent layers to interact with Rh species, suppressing the aggregation and favoring the formation of tiny Rh NPs. Chiral diene ligands with diverse groups create modulated chiral microenvironment to promote enantioselectivity. Accordingly, the optimized Rh–L1@COF achieves high activity and excellent enantioselectivity (up to 95.6 % ee) in asymmetric 1,4-addition reactions between arylboronic acids and nitroalkenes. Though the well-dispersed Rh NPs are beneficial for activity, they are not active themselves until they are decorated with Lx ligands. Moreover, the hydrogen-bonding interaction between L1 and the substrate nitroalkene has been demonstrated to be crucial for the resulting high enantioselectivity.

Results and Discussion

A highly stable 2D mesoporous imide-linked COF constructed by condensing 1,3,5-tris(4-aminophenyl)benzene (TAPB) with 2,5-dimethoxyterephthaldehyde (DMTA) was synthesized in 1,4-dioxane/butanol/methanol (v/v/v, 4:4:1) with 12 M aqueous acetic acid as the modulator at 70 °C for 24 h (Scheme S1).[12] The Rh^{3+} cations were impregnated and inserted into the pre-synthesized TAPB-DMTA-COF (denoted as COF hereafter) through coordination with N atoms between the adjacent layers, followed by H_2 reduction to Rh NPs (Scheme 1). The obtained Rh@COF was then modified with three types of chiral diene ligands, i.e. Lx (x= 1, 2, 3) (Figure S1),[13] to afford Rh–L1@COF, Rh–L2@COF, and Rh–L3@COF, respectively, under stirring in toluene in a nitrogen atmosphere. X-ray photoelectron spectroscopy (XPS) results support the successful coordination of Rh^{3+} by the N atoms between adjacent layers. The N 1s XPS spectrum of Rh^{3+}@COF shows three peaks with binding energies at 395.4 eV, 396.8 eV and 398.2 eV, which can be attributed to free imine N, unreacted amine groups of COF and coordinated imine N, respectively (Figure S2).[14] According to the infrared (IR) spectra, the characteristic peaks assignable to the –N–H– stretch (~3338 cm^{-1}) and –C–N– stretch (~1363 cm^{-1}) for Rh–L1@COF (Figure S3), and the appearance of the –COO– stretch (~1717 cm^{-1}) and –C–N– stretch (~1363 cm^{-1}) for Rh–L2@COF and Rh–L3@COF, respectively (Figures S4, S5), indicate the successful introduction of the chiral ligands Lx into Rh@COF composites. Circular dichroism (CD) spectra reveal the Rh–Lx@COF composites perfectly inherit the chirality of the diene ligands (Figures 1a, S6). XPS spectra for the Rh–Lx@COF composites present two sets of peaks ascribed to Rh^0 and Rh^{3+} in the binding energy range of 304–316 eV (Figure 1b). The presence of Rh^{3+} indicates that the tiny Pd NPs may be partially oxidized in air. Remarkably, the Rh^0 $3d_{5/2}$ peak appears at 306.0 eV in Rh–L1@COF, which is increased by 0.40 eV compared to that in Rh@COF. The positive shift of the Rh^0 $3d_{5/2}$ binding energy suggests the possible coordina-

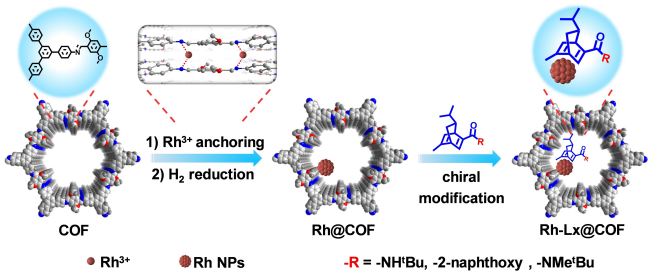

Scheme 1. Illustration showing the synthetic route to Rh–Lx@COF modified with chiral diene ligands (Lx).

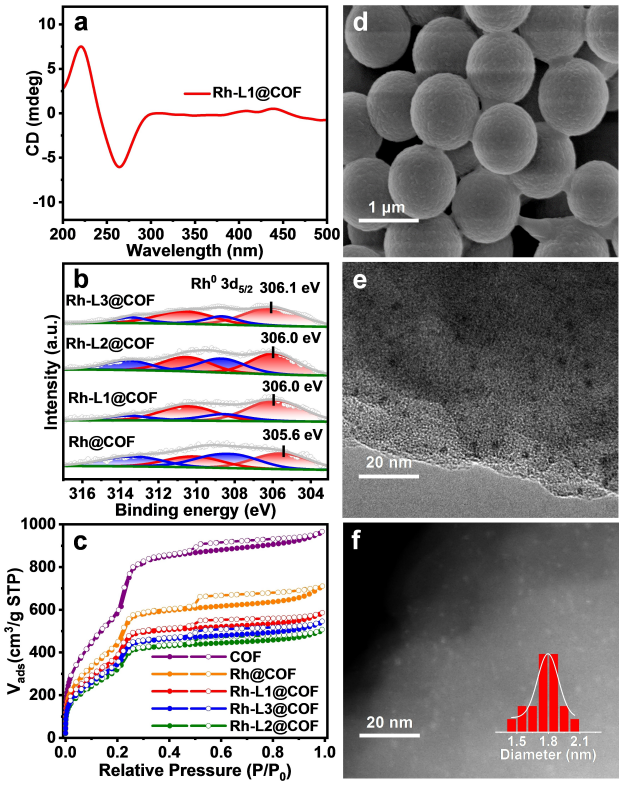

Figure 1. a) CD spectra for Rh–L1@COF. b) XPS spectra of Rh 3d for the Rh@COF and Rh–Lx@COF composites at 298 K. c) Nitrogen sorption isotherms for the COF, Rh@COF, and Rh–Lx@COF samples at 77 K. d) SEM, e) TEM, and f) HAADF-STEM images of Rh–L1@COF (inset: size distribution of the Rh NPs).

© 2024 Wiley-VCH GmbH

RIGHTSLINK

15213773, 2024, 46, Downloaded from https://onlinelibrary.wiley.com/doi/10.1002/anie.202412643 by University Of Science, Wiley Online Library on [04/11/2024]. See the Terms and Conditions (https://onlinelibrary.wiley.com/terms-and-conditions) on Wiley Online Library for rules of use; OA articles are governed by the applicable Creative Commons License

tion of the Rh sites with L1, resulting in an increased oxidation state in the Rh–L1@COF. Similar peak shifts indicate the binding of chiral ligands onto Rh sites in Rh–L2@COF and Rh–L3@COF. UV/Vis spectra demonstrate that Rh@COF showcases far superior adsorption ability for L1 compared to the pristine COF, indicating the good coordination interaction of chiral ligand L1 on the Rh NP surface (Figure S7). Inductively coupled plasma atomic emission spectrometry (ICP-AES) results illustrate that all the samples have similar Rh loadings (1.85–2.17 wt%) (Table S1).

Powder X-ray diffraction (XRD) results suggest that the Rh@COF and Rh–Lx@COF composites inherit phase purity and high crystallinity of the COF very well (Figure S8). Nitrogen sorption isotherms indicate that the Brunauer–Emmett–Teller (BET) surface areas of Rh@COF and Rh–Lx@COF composites reasonably decrease due to the incorporation of Rh NPs and chiral diene ligands compared to the pristine COF (Figure 1c), while the pore size distributions support the retention of porous features (Figure S9). Scanning electron microscopy (SEM) images show that the Rh@COF and Rh–Lx@COF possess uniform spherical morphologies with sizes of ~1.0 μm (Figures 1d, S10). Transmission electron microscopy (TEM) images showcase that the tiny Rh NPs with sizes of ~1.79 nm are dispersed throughout the COF particles (Figures 1e, S11), indicating that no significant change occurs to the Rh NPs during the chiral modification. High-angle annular dark-field scanning transmission electron microscopy (HAADF-STEM) observation for Rh–L1@COF confirms the small sizes of Rh NPs (Figure 1f), and the corresponding elemental mapping results suggest that Rh NPs are uniformly dispersed throughout the Rh–L1@COF particle (Figure S12). The above results unambiguously demonstrate that tiny Rh NPs can be stabilized by the COF confinement, followed by chiral microenvironment modulation of Rh NPs with decoration of diverse chiral diene ligands (Lx).

Asymmetric 1,4-addition reactions between arylboronic acids and nitroalkenes are important asymmetric carbon-carbon bond-forming reactions for the synthesis of chiral drugs.[15] Encouraged by the aforementioned results, the asymmetric 1,4-addition reaction of 3-methoxyphenylboronic acid and (*E*)-*β*-nitrostyrene is chosen to evaluate the catalytic performance over Rh@COF and Rh–Lx@COF composites (Table 1). Significantly, an optimal conversion of 90.5 % with 93.7 % ee can be achieved in 24 h with Rh–L1@COF (Table 1, entry 1; Figures S13, S14). In contrast, Rh–L2@COF affords 63.8 % conversion with 72.8 % ee, and Rh–L3@COF affords 90.3 % conversion with 22.5 % ee under identical conditions (Table 1, entries 2, 3; Figure S14), indicating that chiral microenvironment modulation plays critical roles in the resulting activity and enantioselectivity.

The individual contributions of each component in the catalytic system have been investigated based on control experiments. No target product is detectable in the presence of Rh@COF or chiral diene ligand only (Table 1, entries 4–7), indicating that Rh NPs alone are not able to achieve conversion and that active sites might be on the interface of

Table 1: Asymmetric 1,4-addition reaction between 3-methoxyphenylboronic acid and (*E*)-*β*-nitrostyrene over Rh–Lx@COF with different functional groups and corresponding control catalysts.[a]

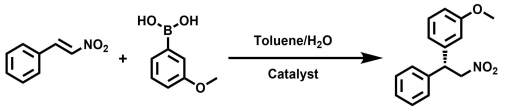

Entry	Catalyst	Conv. (%)	ee (%)
1	Rh–L1@COF	90.5	93.7
2	Rh–L2@COF	63.8	72.8
3	Rh–L3@COF	90.3	22.5
4[b]	Rh@COF	N.D.[c]	/
5[d]	L1	N.D.	/
6[d]	L2	N.D.	/
7[d]	L3	N.D.	/
8[e]	Rh–L1/AC	66.2	91.4
9[e]	Rh–L1/Al_2O_3	72.5	92.6
10[e]	Rh^{3+}–L1	92.4	93.9

[a] Reaction conditions: 0.05 mmol (*E*)-*β*-nitrostyrene, 0.15 mmol 3-methoxyphenylboronic acid, 20.0 mg Rh@COF, 0.007 mmol ligand Lx, 2.5 mL toluene, 0.5 mL H_2O, 100 °C, 24 h, N_2 atmosphere. The conversion was determined by GC, and the ee values were determined by HPLC. [b] Without adding chiral ligand Lx. [c] N.D.: not detectable. [d] Without adding Rh@COF. [e] The Rh sample was added instead of Rh@COF.

Rh NPs coordinated with the Lx ligands. To further demonstrate that the presence of Lx ligand is crucial to switch on the activity, the influence of L1 amount has been investigated with Rh–L1@COF as a representative. The gradual addition of L1 leads to a significant increase in the conversion, indicating a corresponding increase in the number of active sites; in contrast, the ee value remains always high (> 92 %) once L1 is introduced (Table S2). The investigation of H_2O addition reveals that H_2O can favor the hydrolysis of 3-methoxyphenylboronic acid, with the optimal amount significantly enhancing the reaction (Table S3). Given the obviously lower activity of Rh–L2@COF than the other two composites (Table 1, entries 1–3), the addition of triethylamine (TEA) is attempted, and the results suggest the base can markedly promote the conversion without disturbing the enantioselectivity (Table S4). These results suggest that the weak basicity of L1 and L3 might be responsible for accelerating the conversion of the reaction. In addition, Rh–L1/AC (AC means active carbon) and Rh–L1/Al_2O_3 have been prepared as controls following the similar synthetic procedure of Rh–L1@COF. However, the former two composites give much lower conversion (Table 1, entries 8 and 9), which might be attributed to the unavoidable aggregation and the formation of large sizes of Rh NPs loaded on AC and Al_2O_3 (Figures S15, S16). To prove this assumption, the degrees of Rh dispersion in Rh@COF, Rh/Al_2O_3, and Rh/AC have been evaluated using CO chemisorption, with results following the order of Rh@COF > Rh/Al_2O_3 > Rh/AC, which corresponds to the particle sizes observed in the TEM images (Table S5).

Time-dependent conversion experiments show that high enantioselectivity can be maintained with Rh–L1@COF throughout the reaction process (Figure S17). Both Rh–L1/

© 2024 Wiley-VCH GmbH

15213773, 2024, 46, Downloaded from https://onlinelibrary.wiley.com/doi/10.1002/anie.202412643 by University Of Science, Wiley Online Library on [04/11/2024]. See the Terms and Conditions (https://onlinelibrary.wiley.com/terms-and-conditions) on Wiley Online Library for rules of use; OA articles are governed by the applicable Creative Commons License

RIGHTSLINK

AC and Rh–L1/Al_2O_3 present stably high enantioselectivity yet lower kinetic conversion than Rh–L1@COF. The direct comparison highlights the unique advantage of COF stabilizing tiny Rh NPs toward high activity (Figures S18, S19). To verify the heterogeneous nature of the Rh–L1@COF catalyst, the hot filtration experiment and nonlinear effect (NLE) analysis[16] have been executed (Figure 2). The result indicates that no further reaction occurs when the catalyst is filtered out at 4 h (Figure 2a), confirming the heterogeneous nature of the catalytic process. Negligible leaching of Rh species is observed for Rh–L1@COF based on the ICP results (Table S1, entry 7). Based on the NLE analysis over Rh–L1@COF and Rh^{3+}–L1, the homogeneous Rh^{3+}–L1 showcases not only a high activity and ee but also an approximately linear relation between the chiral purity (ee value) of the L1 ligand and the product (Table 1, entry 10, Figure 2b). In contrast, the NLE curve for Rh–L1@COF gives a classical arched curve (Figure 2b). This direct comparison indicates that although the modification of Rh NPs with L1 ligand is essential to initiate the activity (Table 1, entries 1–4), the active sites in Rh–L1@COF and Rh^{3+}-L1 are distinctly different. This difference further highlights the heterogeneous nature of the Rh–L1@COF catalyst. To evaluate the stability of Rh–L1@COF, recycling experiments demonstrate that conversion efficiency and enantioselectivity can be well maintained after five consecutive runs with additional L1 (Figures S20, S21). Moreover, the powder XRD pattern suggests that Rh–L1@COF maintains structural integrity and high crystallinity after the catalytic reaction and recycling (Figure S22). SEM image shows the spherical morphology of Rh–L1@COF is preserved (Figure S23). The good dispersion of the Rh NPs throughout the COF particles can be observed by TEM after the reaction (Figure S24). XPS results reveal that Rh NPs are further oxidized upon exposure to air in reaction, while the Rh–L1 sites remain stable during reaction (Figure S25). Moreover, IR and CD spectra further support the structure and chirality are retained for Rh–L1@COF after reaction (Figures S26, S27). Under the optimized conditions, a wide range of arylboronic acids and nitroalkenes have been investigated over Rh–L1@COF (Table 2). To our delight, good conversion and high enantioselectivities can be obtained for diverse substrates bearing either electron-withdrawing or -donating groups, reflecting the good substrate tolerance of Rh–L1@COF.

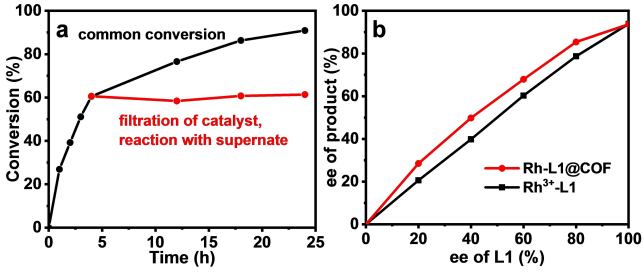

Figure 2. a) Time-dependent conversion and hot filtration test of the asymmetric 1,4-addition reaction between 3-methoxyphenylboronic acid and (*E*)-*β*-nitrostyrene over Rh–L1@COF. b) Nonlinear effects of Rh^{3+}–L1 complex and Rh–L1@COF for asymmetric 1,4-addition reaction between 3-methoxyphenylboronic acid and (*E*)-*β*-nitrostyrene.

Table 2: Substrate scope for asymmetric 1,4-addition reactions between arylboronic acids and nitroalkenes catalyzed by Rh–L1@COF.[a]

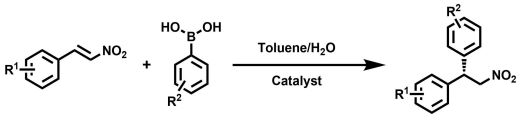

Entry	R^1	R^2	Conv. (%)	ee (%)
1	H	3-MeO	90.5	93.7
2	H	4-F	92.3	90.6
3	H	4-Me	93.7	89.1
4	H	4-MeO	92.3	89.4
5	4-MeO	4-Me	90.2	92.3
6	4-MeO	3-MeO	91.4	94.5
7	4-F	3-MeO	94.2	95.2
8	4-Cl	3-MeO	93.2	92.1
9	4-Br	3-MeO	91.5	89.9
10	3,4-$(MeO)_2$	H	93.5	95.6

[a] Reaction conditions: 0.05 mmol nitrostyrene, 0.15 mmol boronic acid, 20.0 mg Rh@COF, 0.007 mmol L1, 2.5 mL toluene, 0.5 mL H_2O, 100 °C, 24 h, N_2 atmosphere. The conversion was determined by GC, and the ee value was determined by HPLC.

The possible reaction pathway for the asymmetric 1,4-addition reaction between 3-methoxyphenylboronic acid and (*E*)-*β*-nitrostyrene over Rh–L1@COF has been analyzed (Figure S28).[15a] Typically, 3-methoxyphenylboronic acid undergoes hydrolysis to generate an intermediate that is adsorbed on the surface of Rh NPs (Figure S28, I→II), as evidenced by the detection of an anisole byproduct (Figure S29). Subsequently, the 3-methoxyaryl intermediate is nucleophilically added to the β position of (*E*)-*β*-nitrostyrene due to the electron-withdrawing effect of nitro group, and both the bicyclo[2.2.2]octadiene skeleton and functional groups play significant roles in inducing the chirality of the addition intermediate (Figure S28, II→III and III→IV).

To elucidate the mechanism behind the high enantioselectivity, it is necessary to investigate the potential interactions between the Lx ligands and substrates. The chirality of the Lx ligands originates from the bicyclo[2.2.2]octadiene structure,while tunable functional groups might modulate the spatial configuration of reaction intermediates through weak interactions to improve enantioselectivity. In our system, L1 bearing a tert-butyl amide can serve as the hydrogen donor, and (*E*)-*β*- nitrostyrene acts as the hydrogen acceptor (Figure 3a), thereby forming hydrogen-bonding interactions during the reaction process. Based on the concentration-dependent ^{1}H nuclear magnetic resonance (^{1}H NMR) tests, the chemical shift of the active hydrogen shifts to a lower field upon the formation of hydrogen bonds.[17] The chemical shift of active hydrogen of tert-butyl amide shifts from 5.51 to 5.59 ppm when using a fixed concentration of L1 ligand as a probe molecule and increasing the concentration of (*E*)-*β*-nitrostyrene, indicating the formation of hydrogen bonds (Figures 3b, S30). In contrast, in the case of L2 and L3 ligands, there are no potential sites for the formation of hydrogen bonds with

© 2024 Wiley-VCH GmbH

15213773, 2024, 46, Downloaded from https://onlinelibrary.wiley.com/doi/10.1002/anie.202412643 by University Of Science, Wiley Online Library on [04/11/2024]. See the Terms and Conditions (https://onlinelibrary.wiley.com/terms-and-conditions) on Wiley Online Library for rules of use; OA articles are governed by the applicable Creative Commons License

RIGHTSLINK

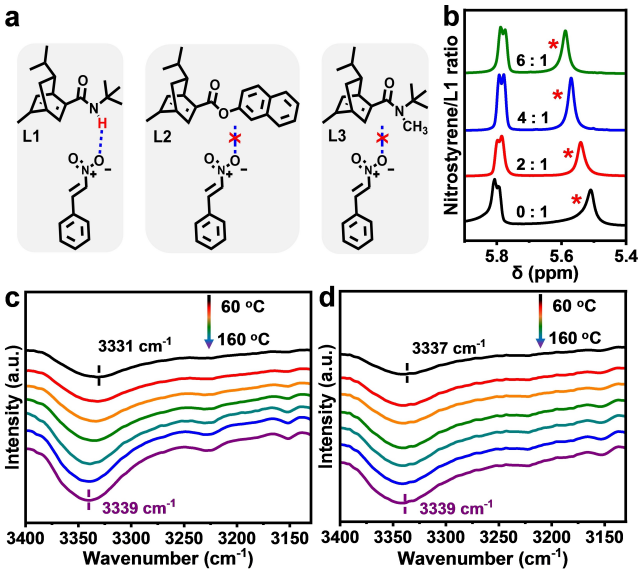

Figure 3. a) Illustration showing the possible hydrogen-bonding interactions between L1 and (*E*)-*β*-nitrostyrene, whereas there are no such interaction between L2, L3, and the substrate. b) Partially amplified ^{1}H NMR spectra of L1 with different concentrations of (*E*)-*β*-nitrostyrene. Temperature-dependent DRIFTS spectra for c) Rh–L1@COF with (*E*)-*β*-nitrostyrene and d) Rh–L1@COF at increasing temperatures from 60 to 160 °C.

(*E*)-*β*-nitrostyrene; accordingly, the reactions achieve lower enantioselectivities. The capacity for chiral induction follows the order of Rh–L1@COF > Rh–L2@COF > Rh–L3@COF, highlighting the important role of hydrogen-bonding interactions in enantioselectivity control. The bulky groups in L2 and L3 suggest that a large steric hindrance is favorable for enantioselectivity; the integration of this steric hindrance and hydrogen-bonding interactions in L1 is able to provide optimal results.

Temperature-dependent diffuse reflectance infrared Fourier transform spectroscopy (DRIFTS) has been employed to further investigate the hydrogen-bonding interactions in the catalytic system in the presence of Rh–L1@COF and (*E*)-*β*-nitrostyrene from 60 to 160 °C.[18] The characteristic peak attributed to the -N–H stretch shifts from 3331 cm^{-1} to 3339 cm^{-1} with increasing temperature (Figure 3c), indicating that the strength of the hydrogen-bonding interaction gradually decreases. To our delight, although the strength at 100 °C is relatively weaker than that at 60 °C, hydrogen-bonding interactions do occur between L1 ligand and (*E*)-*β*-nitrostyrene under reaction conditions (100 °C). As a control, the shift of Rh–L1@COF without the addition of (*E*)-*β*-nitrostyrene has also been studied. The peak of the –N–H stretch shifts from 3337 to 3339 cm^{-1} with increasing temperature from 60 to 160 °C (Figure 3d), suggesting a negligible peak shift. Both concentration-dependent ^{1}H NMR and temperature-dependent DRIFTS discussed above provide solid experimental evidences on the presence of hydrogen-bonding interactions between L1 ligand and the substrate. In addition, the dramatically reduced ee (22.5 %) for Rh–L3@COF, as a direct comparison, unambiguously elucidates that the hydrogen-bonding interactions play a crucial role in promoting enantioselectivity of the reaction at 100 °C.

Conclusion

In summary, tiny Rh NPs have been encapsulated in COFs, followed by modifying Rh NPs with diverse chiral diene ligands, to afford Rh–Lx@COF for asymmetric 1,4-addition reactions between arylboronic acids and nitroalkenes. The N atoms from adjacent layers interact with and prevent agglomeration of the Rh species, leading to the formation of small Rh NPs and improved conversion. The decoration of chiral diene ligands on the Rh NPs not only creates particular chiral microenvironment around Rh NPs responsible for the product enantioselectivity, but also initiates the activity, in sharp contrast to the inactivity of Rh NPs alone, which eliminates the background reaction commonly observed in previous reports on chiral ligands modified on metal NPs. The group variation on the chiral diene ligands can modulate the chiral microenvironment and hydrogen-bonding interactions, further regulating the product enantioselectivity. As a result, the optimized Rh–L1@COF achieves high activity and excellent enantioselectivity (up to 95.6 % ee), while Rh–L2@COF bearing bulky 2-naphthoxy produces medium enantioselectivity (72.8 % ee), in comparison to Rh–L3@COF (22.5 % ee). This work not only opens up an avenue to the fabrication of chiral heterogeneous metal catalysts by simple modification of chiral ligands onto metal NPs, but also paves the way for supported metal catalysts toward heterogeneous asymmetric catalysis.

Acknowledgements

This work is supported by the National Key Research and Development Program of China (2021YFA1500400), National Natural Science Foundation of China (22331009 and 22101269), the Strategic Priority Research Program of the Chinese Academy of Sciences (XDB0450302, XDB0540000) and the Fundamental Research Funds for the Central Universities (WK2060000038). This work was partially carried out at the Instruments Center for Physical Science, University of Science and Technology of China.

Conflict of Interest

The authors declare no conflict of interest.

Data Availability Statement

The data that support the findings of this study are available from the corresponding author upon reasonable request.

© 2024 Wiley-VCH GmbH

15213773, 2024, 46, Downloaded from https://onlinelibrary.wiley.com/doi/10.1002/anie.202412643 by University Of Science, Wiley Online Library on [04/11/2024]. See the Terms and Conditions (https://onlinelibrary.wiley.com/terms-and-conditions) on Wiley Online Library for rules of use; OA articles are governed by the applicable Creative Commons License

RIGHTSLINK

Keywords: covalent organic frameworks · metal nanoparticle · heterogeneous asymmetric catalysis · microenvironment modulation

[1] a) J. R. Brandt, F. Salerno, M. J. Fuchter, *Nat. Chem. Rev.* **2017**, *1*, 0045; b) X. Han, C. Yuan, B. Hou, L. Liu, H. Li, Y. Liu, Y. Cui, *Chem. Soc. Rev.* **2020**, *49*, 6248–6272.

[2] a) L.-W. Xu, J. Luo, Y. Lu, *Chem. Commun.* **2009**, 1807–1821; b) S. Shaw, J. D. White, *Chem. Rev.* **2019**, *119*, 9381–9426; c) Z.-L. Xia, Q.-F. Xu-Xu, C. Zheng, S.-L. You, *Chem. Soc. Rev.* **2020**, *49*, 286–300.

[3] a) Q. Han, C. He, M. Zhao, B. Qi, J. Niu, C. Duan, *J. Am. Chem. Soc.* **2013**, *135*, 10186–10189; b) L. Ma, C. Abney, W. Lin, *Chem. Soc. Rev.* **2009**, *38*, 1248–1256; c) H.-C. Ma, J. Zou, X.-T. Li, G.-J. Chen, Y.-B. Dong, *Chem. Eur. J.* **2020**, *26*, 13754–13770; d) H. Dai, Q. Yang, *Chem Catal.* **2022**, *2*, 2840–2851.

[4] a) Y. Zhang, S. Chen, A. M. Al-Enizi, A. Nafady, Z. Tang, S. Ma, *Angew. Chem. Int. Ed.* **2023**, *62*, e202213399; b) H. Ishitani, K. Kanai, W.-J. Yoo, T. Yoshida, S. Kobayashi, *Angew. Chem. Int. Ed.* **2019**, *58*, 13313–13317; c) M. Yoon, R. Srirambalaji, K. Kim, *Chem. Rev.* **2012**, *112*, 1196–1231.

[5] a) T. P. Yoon, E. N. Jacobsen, *Science* **2003**, *299*, 1691–1693; b) H. Yang, L. Zhang, L. Zhong, Q. Yang, C. Li, *Angew. Chem. Int. Ed.* **2007**, *46*, 6861–6865; c) W. Gong, X. Chen, K. M. Fahy, J. Dong, Y. Liu, O. K. Farha, Y. Cui, *J. Am. Chem. Soc.* **2023**, *145*, 13869–13878; d) H. Xu, J. Gao, D. Jiang, *Nat. Chem.* **2015**, *7*, 905–912.

[6] a) S. J. Benkovic, S. Hammes-Schiffer, *Science* **2003**, *301*, 1196–1202; b) A. R. Riscoe, C. J. Wrasman, A. A. Herzing, A. S. Hoffman, A. Menon, A. Boubnov, M. Vargas, S. R. Bare, M. Cargnello, *Nat. Catal.* **2019**, *2*, 852–863; c) G. Yang, W. Shi, Y. Qian, X. Zheng, Z. Meng, H.-L. Jiang, *Angew. Chem. Int. Ed.* **2023**, *62*, e202308089; d) Q. Sun, C.-W. Fu, B. Aguila, J. Perman, S. Wang, H.-Y. Huang, F.-S. Xiao, S. Ma, *J. Am. Chem. Soc.* **2018**, *140*, 984–992.

[7] a) F. Meemken, A. Baiker, *Chem. Rev.* **2017**, *117*, 11522–11569; b) Z. Du, C. Liu, H. Song, P. Scott, Z. Liu, J. Ren, X. Qu, *Chem* **2020**, *6*, 2060–2072; c) T. Yasukawa, H. Miyamura, S. Kobayashi, *J. Am. Chem. Soc.* **2012**, *134*, 16963–16966; d) N. Bonalumi, T. Bürgi, A. Baiker, *J. Am. Chem. Soc.* **2003**, *125*, 13342–13343; e) I. Schrader, J. Warneke, J. Backenkoehler, S. Kunz, *J. Am. Chem. Soc.* **2015**, *137*, 905–912; f) E. Gross, J. H. Liu, S. Alayoglu, M. A. Marcus, S. C. Fakra, F. D. Toste, G. A. Somorjai, *J. Am. Chem. Soc.* **2013**, *135*, 3881–3886; g) Y. Zhou, H. Sun, H. Xu, S. Matysiak, J. Ren, X. Qu, *Angew. Chem. Int. Ed.* **2018**, *57*, 16791–16795; h) X. Gao, X. Chen, Z. H. Li, H. He, *ACS Catal.* **2019**, *9*, 6100–6110; i) Y. Ren, M. Wang, Q. Yang, J. Zhu, *ACS Catal.* **2023**, *13*, 1974–1982.

[8] a) Q. Yang, Q. Xu, H.-L. Jiang, *Chem. Soc. Rev.* **2017**, *46*, 4774–4808; b) L. Liu, J. Lu, Y. Yang, W. Ruettinger, X. Gao, M. Wang, H. Lou, Z. Wang, Y. Liu, X. Tao, L. Li, Y. Wang, H. Li, H. Zhou, C. Wang, Q. Luo, H. Wu, K. Zhang, J. Ma, X. Cao, L. Wang, F.-S. Xiao, *Science* **2024**, *383*, 94–101; c) X. C. Pei, S. Chen, D. Fu, Z.-J. Zhao, J. Gong, *Chem. Rev.* **2024**, *124*, 2955–3012; d) X. Zhu, Q. Guo, Y. Sun, S. Chen, J. Q. Wang, M. Wu, W. Fu, Y. Tang, X. Duan, D. Chen, Y. Wan, *Nat. Commun.* **2019**, *10*, 1428; e) K. L. Kollmannsberger, L. Kronthaler, J. R. Jinschek, R. A. Fischer, *Chem. Soc. Rev.* **2022**, *51*, 9933–9959; f) G. Li, S. Zhao, Y. Zhang, Z. Tang, *Adv. Mater.* **2018**, *30*, 1800702.

[9] a) A. P. Côté, A. I. Benin, N. W. Ockwig, M. O'Keeffe, A. J. Matzger, O. M. Yaghi, *Science* **2005**, *310*, 1166–1170; b) K. Geng, T. He, R. Liu, S. Dalapati, K. T. Tan, Z. Li, S. Tao, Y. Gong, Q. Jiang, D. Jiang, *Chem. Rev.* **2020**, *120*, 8814–8933; c) Q. Zhang, S. Dong, P. Shao, Y. Zhu, Z. Mu, D. Sheng, T. Zhang, X. Jiang, R. Shao, Z. Ren, J. Xie, X. Feng, B. Wang, *Science* **2022**, *378*, 181–186; d) J. Chang, F. Chen, H. Li, J. Suo, H. Zheng, J. Zhang, Z. Wang, L. Zhu, V. Valtchev, S. Qiu, Q. Fang, *Nat. Commun.* **2024**, *15*, 813; e) C. Kang, Z. Zhang, S. Kusaka, K. Negita, A. K. Usadi, D. C. Calabro, L. S. Baugh, Y. Wang, X. Zou, Z. Huang, R. Matsuda, D. Zhao, *Nat. Mater.* **2023**, *22*, 636–643; f) T. He, R. Liu, S. Wang, I. K. W. On, Y. Wu, Y. Xing, W. Yuan, J. Guo, Y. Zhao, *J. Am. Chem. Soc.* **2023**, *145*, 18015–18021; g) Y. Qian, H.-L. Jiang, *Acc. Mater. Res.* **2024**, *57*, 1214–1226; h) H.-S. Xu, S.-Y. Ding, W.-K. An, H. Wu, W. Wang, *J. Am. Chem. Soc.* **2016**, *138*, 11489–11492; i) C. Li, L. Guan, J. Zhang, C. Cheng, Z. Guo, Z. Tian, L.-M. Yang, S. Jin, *J. Mater. Chem. A* **2024**, *12*, 13876–13881; j) H. Zhuang, C. Guo, J. Huang, L. Wang, Z. Zheng, H.-N. Wang, Y. Chen, Y.-Q. Lan, *Angew. Chem. Int. Ed.* **2024**, e202404941.

[10] a) S. Lu, Y. Hu, S. Wan, R. McCaffrey, Y. Jin, H. Gu, W. Zhang, *J. Am. Chem. Soc.* **2017**, *139*, 17082–17088; b) P. Pachfule, M. K. Panda, S. Kandambeth, S. M. Shivaprasad, D. D. Díaz, R. Banerjee, *J. Mater. Chem. A* **2014**, *2*, 7944–7952; c) M. Guo, Q. Meng, W. Chen, Z. Meng, M.-L. Gao, Q. Li, X. Duan, H.-L. Jiang, *Angew. Chem. Int. Ed.* **2023**, *62*, e202305212; d) M. Guo, S. Jayakumar, M. Luo, X. Kong, C. Li, H. Li, J. Chen, Q. Yang, *Nat. Commun.* **2022**, *13*, 1770.

[11] a) S.-Y. Ding, J. Gao, Q. Wang, Y. Zhang, W.-G. Song, C.-Y. Su, W. Wang, *J. Am. Chem. Soc.* **2011**, *133*, 19816–19822; b) I. Romero-Muñiz, A. Mavrandonakis, P. Albacete, A. Vega, V. Briois, F. Zamora, A. E. Platero-Prats, *Angew. Chem. Int. Ed.* **2020**, *59*, 13013–13020.

[12] X. Shi, Y. Yao, Y. Xu, K. Liu, G. Zhu, L. Chi, G. Lu, *ACS Appl. Mater. Interfaces* **2017**, *9*, 7481–7488.

[13] a) T. Hayashi, K. Ueyama, N. Tokunaga, K. Yoshida, *J. Am. Chem. Soc.* **2003**, *125*, 11508–11509; b) K. Okamoto, T. Hayashi, V. H. Rawal, *Org. Lett.* **2008**, *10*, 4387–4389.

[14] a) L. Lai, L. Chen, D. Zhan, L. Sun, J. Liu, S. H. Lim, C. K. Poh, Z. Shen, J. Lin, *Carbon* **2011**, *49*, 3250–3257; b) J. Hu, H. Mehrabi, Y.-S. Meng, M. Taylor, J.-H. Zhan, Q. Yan, M. Benamara, R. H. Coridan, H. Beyzavi, *Chem. Sci.* **2021**, *12*, 7930–7936.

[15] a) Z.-Q. Wang, C.-G. Feng, S.-S. Zhang, M.-H. Xu, G.-Q. Lin, *Angew. Chem. Int. Ed.* **2010**, *49*, 5780–5783; b) K. Zheng, X. Liu, X. Feng, *Chem. Rev.* **2018**, *118*, 7586–7656; c) T. Kuremoto, T. Yasukawa, S. Kobayashi, *Adv. Synth. Catal.* **2019**, *361*, 3698–3703.

[16] T. Satyanarayana, S. Abraham, H. B. Kagan, *Angew. Chem. Int. Ed.* **2009**, *48*, 456–494.

[17] a) Y. Luo, H. Ma, S. Zhang, D. Zheng, P. Che, X. Liu, M. Zhang, J. Gao, J. Xu, *J. Am. Chem. Soc.* **2020**, *142*, 6085–6092; b) S. Shi, P. Yang, C. Dun, W. Zheng, J. J. Urban, D. G. Vlachos, *Nat. Commun.* **2023**, *14*, 429.

[18] N. V. Belkova, E. I. Gutsul, O. A. Filippov, V. A. Levina, D. A. Valyaev, L. M. Epstein, A. Lledos, E. S. Shubina, *J. Am. Chem. Soc.* **2006**, *128*, 3486–3487.

Manuscript received: July 5, 2024
Accepted manuscript online: August 5, 2024
Version of record online: September 20, 2024

© 2024 Wiley-VCH GmbH

15213773, 2024, 46, Downloaded from https://onlinelibrary.wiley.com/doi/10.1002/anie.202412643 by University Of Science, Wiley Online Library on [04/11/2024]. See the Terms and Conditions (https://onlinelibrary.wiley.com/terms-and-conditions) on Wiley Online Library for rules of use; OA articles are governed by the applicable Creative Commons License

RIGHTSLINK